Nanoscale

PAPER

View Article Online
View Journal | View Issue

Cite this: *Nanoscale*, 2019, **11**, 7256

A 2D nonsymmorphic Dirac semimetal in a chemically modified group-VA monolayer with a black phosphorene structure†

Kyung-Hwan Jin, [a] Huaqing Huang,[a] Zhengfei Wang [b] and Feng Liu*[a,c]

A symmetry-protected 2D Dirac semimetal has attracted intense interest for its intriguing material properties. Here, we report a 2D nonsymmorphic Dirac semimetal state in a chemically modified group-VA 2D puckered structure. Based on first-principles calculations, we demonstrate the existence of 2D Dirac fermions in a one-side modified phosphorene structure in two different types: one with a Dirac nodal line (DNL) structure for light elements with negligible spin–orbit coupling (SOC) and the other having an hourglass band protected by a nonsymmorphic symmetry for heavy elements with strong SOC. In the absence of SOC, the DNL exhibits an anisotropic behavior and unique electronic properties, such as constant density of states. The Dirac node is protected from gap opening by the nonsymmorphic space group symmetry. In the presence of SOC, the DNL states split and form an hourglass-shaped dispersion due to the broken inversion symmetry and the Rashba SOC interaction. Moreover, around certain high symmetry points in the Brillouin zone, the spin orientation is enforced to be along a specific direction. We construct an effective tight-binding model to characterize the 2D nonsymmorphic Dirac states. Our result provides a promising material platform for exploring the intriguing properties of essential nodal-line and nodal-point fermions in 2D systems.

Received 28th January 2019,
Accepted 17th March 2019

DOI: 10.1039/c9nr00906j

rsc.li/nanoscale

Introduction

Over the past decade, there has been a dramatic surge in the study of Dirac fermions in condensed matter systems, ranging from graphene,[1] topological insulators[2] to Dirac and Weyl semimetals,[3,4] which possess a number of unique electronic properties owing to their relativistic band dispersions and chiral/helical transport properties. In particular, graphene has become the prototypical model system of two-dimensional (2D) Dirac fermions protected by lattice symmetry. On the other hand, spin–orbit coupling (SOC) opens a gap at the Dirac point, leading to a quantum spin Hall phase.[5] Recently, new concepts of 2D Dirac semimetals, which feature Dirac points that are not gapped by SOC interaction, are introduced with a nonsymmorphic symmetry.[6] However, the 2D nonsymmorphic Dirac semimetal in realistic materials has been rarely reported in the literature.[7]

Black phosphorus has gained a lot of recent attention as a new 2D layered system.[8–12] In particular, the exploration of 2D materials built from single-layer black phosphorus, phosphorene, has been extended to other group-VA elements (As, Sb and Bi).[13–19] The phosphorene has a puckered lattice structure and a semiconducting band gap with good carrier mobility. Due to strong in-plane anisotropy, such structures show anisotropic electronic, transport and optical properties.[8,20–22] Recently, a single- or few-monolayer puckered structure for Sb and Bi grown on a suitable substrate has been realized experimentally.[18,19] Moreover, a buckled structure with group-VA elements has attracted attention as it is predicted and confirmed to be a quantum spin Hall state with well-localized nontrivial edge states.[23–32] Beyond these previous experimental and theoretical studies, we are particularly interested in the structures made of group-VA elements to realize new types of 2D Dirac semimetals due to the unique underlying honeycomb symmetry of the puckered structure. Moreover, we will manipulate their electronic band structures and topological states by surface adsorption, which can be achieved in the post synthesis process.[33–35]

We investigate the 2D nonsymmorphic Dirac semimetal state in the chemically modified group-VA 2D puckered struc-

[a]*Department of Materials Science and Engineering, University of Utah, Salt Lake City, UT 84112, USA. E-mail: fliu@eng.utah.edu*
[b]*Hefei National Laboratory for Physical Sciences at the Microscale, University of Science and Technology of China, Hefei, Anhui 230026, China*
[c]*Collaborative Innovation Center of Quantum Matter, Beijing 100084, China*

†Electronic supplementary information (ESI) available: Calculated lattice parameters and formation energy, phonon band structure, tight binding model, plasmon excitation, band structure without SOC, the variation of DOS in Bi–F and the vdW heterostructure of As–F and BN sheets. See DOI: 10.1039/c9nr00906j

ture. Based on the symmetry analysis and first-principles calculations, we demonstrate that 2D Dirac fermion states not only exist in a one-side modified phosphorene structure, but also in fact occur in two different types: one has a Dirac nodal line (DNL) structure for light elements with negligible SOC, while the other type has an hourglass fermion state protected by a nonsymmorphic symmetry for heavy elements with strong SOC. In the absence of SOC, the band crossing occurs at the zone boundary with time-reversal symmetry and the DNL exhibits anisotropic behavior and unique electronic properties, such as constant density of states (DOS). In the presence of SOC, the DNL states split and form the essential hourglass dispersion due to the breaking of inversion symmetry and the Rashba SOC interaction. We show that this interesting type of band crossing is protected and dictated by the nonsymmorphic space group symmetries. Moreover, around certain high symmetry points in the Brillouin zone (BZ), the spin orientation is enforced to be along one specific direction. The symmetry-imposed spin texture survives over the large part of BZ. The essential physics of 2D nonsymmorphic Dirac states is further analyzed by effective tight-binding models and group theory.

Methods

The density functional theory (DFT) calculations were carried out using the Vienna *ab initio* simulation package, at the level of the generalized-gradient approximation (GGA).[36,37] We used the projector augmented wave method for the description of the core–valence interaction. A vacuum space of 20 Å was employed to ensure decoupling between neighboring layers. All the calculations were carried out with a kinetic energy cutoff of 500 eV and a 15 × 15 × 1 Monkhorst–Pack k-point mesh. All the structures were fully optimized until the residual forces were less than 0.01 eV Å^{-1}. The SOC was included in the self-consistent electronic structure calculation. The expected values of the spin operators $s_i = \langle\psi_k|\sigma_i|\psi_k\rangle$ (i = x,y,z) were obtained directly from the noncolinear DFT calculations. Phonon dispersions were obtained by using the frozen phonon method as implemented in the PHONOPY code.[38]

Results and discussion

We first discuss the mechanism of bond formation in a group VA phosphorene structure with adatoms (H, F, Cl and Br). The phosphorene structure is represented as chains of covalently bonded group VA atoms lying in two different planes. The VA atoms in a chain within one plane are covalently bonded with the atoms in the other plane [Fig. 1(a)]. Each VA atom assumes an sp^3 orbital hybridization in a tetrahedral bonding geometry. Three electrons participate in forming three covalent σ-bonds with neighboring atoms, whereas two other electrons form a lone pair oriented out of plane. Adatoms on one side of the VA

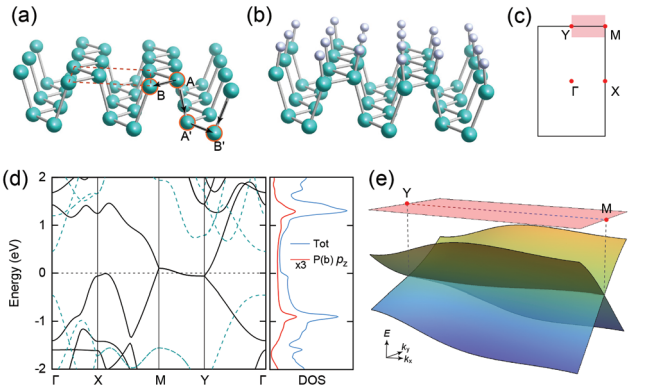

Fig. 1 Atomic structures of (a) the pristine group VA phosphorene structure and (b) the atom decorated phosphorene type structure. (c) The Brillouin zone with high-symmetric points. (d) The band structure for pristine (dashed line) and F-decorated phosphorene (P–F). (e) The DNL structure along the Y–M direction as indicated by a small shaded rectangle in (c).

phosphorene structure are placed on VA atoms [Fig. 1(b)]. In low coverage, the adatoms we chose prefer to be on the top of the VA atom.[39] The first BZ of the pristine and functionalized VA structure is shown in Fig. 1(c). The calculated geometric parameters of the atomic functionalized group VA phosphorene structure are summarized in Table S1.† We also calculated the phonon dispersion and formation energy to check the stability of the functionalized group VA phosphorene structure (Fig. S1 and Table S2†). The structure is found stable even without the long-wavelength buckling instability of the monolayer structure.[40] With the adatoms, the space group of the initial phosphorene structure *Pmna* (no 53) changes to *Pma*2 (no 28). The nonsymmorphic space group *Pma*2 of the functionalized group VA phosphorene structure contains several symmetry operations of glide planes and screw axes (see Table 1).

Most of the 2D materials are grown or exfoliated on a suitable substrate, and they are found to be stable in freestanding form. Thus, we studied single sided functionalization on the group VA phosphorene structure, which is found also to be stable. The single-side modified phosphorene induces significant changes in the electronic structure. Let us first consider an F-decorated phosphorene (P–F) structure. Fig. 1(d) and (e) show the band structure of P–F. The band structure exhibits linear dispersions at both Y and M points. The semimetallic

Table 1 Symmetries of the atom-functionalized group VA phosphorene structure with the nonsymmorphic space-group *Pma*2 (no 28)

Symmetry	(x,y,z) form	Operation
Identity	(x,y,z)	$\{1\|0\}$
Glide plane	($-x$,y + 1/2,z)	$\{M_{100}\|0,1/2,0\}$
Glide plane	(x,$-y$ + 1/2,z)	$\{M_{010}\|0,1/2,0\}$
Rotation	($-x$,$-y$,z)	$\{2_{001}\|0\}$

behavior of pristine phosphorene becomes metallic. Remarkably, the Dirac bands are dispersive along the Y to M directions, so that we have a dispersive DNL structure [Fig. 1(e)]. The emerged DNL structure originated from the π-electrons of phosphorus chains in the bottom plane. One σ-orbital forms a covalent bond with the adatom, and two others form covalent bonds with phosphorus atoms in the top plane [Fig. 2(a)]. Furthermore, the lone pair points towards the bottom phosphorus plane. The covalent bond in between the phosphorus planes turns out to be broken with the increased distance between the top and the bottom layer. The breakage of covalent bonds induces an sp^3 to sp^2 transition in the bottom plane, which transforms itself into phosphorus chains. We plotted the partial charge density of the DNL states. As shown in Fig. 2(b) and (c), the DNL states mainly originated from the p_z orbitals of P atoms in the unsaturated layer.

Moreover, one can better understand the bonding nature and band evolution using a tight-binding (TB) model. The TB Hamiltonian is represented as a 16 × 16 matrix, in which the Bloch sums of s, p_x, p_y and p_z orbitals at A, B, A′ and B′ sites are taken as the bases [Fig. 1(a) and the ESI†]. The Hamiltonian gives the band dispersion of phosphorene using appropriate parameters, as shown in Fig. 2(d). We can see that sixteen bands are divided into eight pairs. The lowest two pairs, three pairs below the gap, and three pairs above the gap can be regarded at the s-bonding and -antibonding bands, p-bonding and -antibonding bands, respectively. One can define the hopping strength κ (= t'_i/t_i, i = spσ, ppσ, ppπ) between the p_z orbitals of the A (B) site and s, p_x, p_y, p_z orbitals of the A′(B′) site, and *vice versa*: for κ = 1, the interlayer hopping is strong; for κ = 0, it mitigates the p_z-orbital-involved hopping interactions between the interlayers. If we tune the κ from 1 to 0, the band gap decreases and the DNL forms along the Y to M direction. As the p_z-orbital-involved interlayer interaction is eliminated, the p_z orbital hopping exists solely in the zigzag chain within each layer.

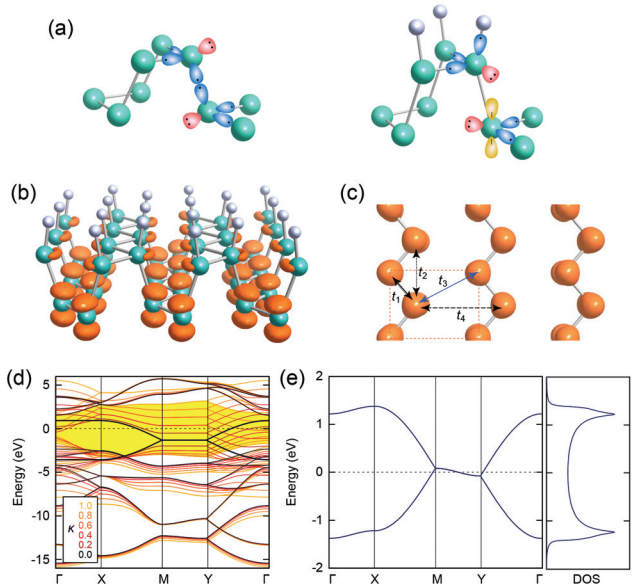

Fig. 2 (a) Schematic view of sp^3 hybridization for the pristine phosphorene structure (left) and of sp^3–sp^2 hybridization for the atom functionalized phosphorene structure (right). Blue, red and yellow lobes represent σ-bonding orbitals, lone pairs and π-bonding orbitals, respectively. The squared wave functions of the Dirac point states with (b) the perspective view and (c) the top view (top layer is removed). (d) The TB band structures with the varying hopping strength κ. (e) The band structure of the effective Hamiltonian using two p_z orbitals with the hopping parameter t_1 = −0.65 eV, t_2 = t_3 = 0 eV and t_4 = −0.04 eV.

The essential physics of the DNL structure in P–F is further characterized by an effective TB model using two P p_z orbitals in a rectangular lattice [Fig. 2(c)]. The p_z bands of P–F have a 2D nature, because there is hopping interaction not only between intra-chain P–P bonds (t_1) but also between inter-chain P–P bonds (t_4). The inter-chain P–P bonds are much larger than the intra-chin P–P bonds, and hence the P–P bonding is strongly anisotropic. Thus we can construct the spinless effective TB Hamiltonian as

$$H = h_0\sigma_0 + h_1\sigma_1 + h_2\sigma_2, \quad (1)$$

where the matrix elements are

$$\begin{aligned} h_0 &= 2t_2\cos(bk_y) + 2t_4\cos(ak_x) \\ h_1 &= 2\cos(\delta k_y)[t_1\cos(ak_x) + t_3\cos((\gamma - a)k_x)] \\ h_2 &= -2\cos(\delta k_y)[t_1\sin(ak_x) + t_3\sin((\gamma - a)k_x)], \end{aligned} \quad (2)$$

a and b are the lattice constants of the rectangular lattice with atomic positions (0,0) and (γ,δ). Fig. 2(e) shows the band structure of an effective Hamiltonian with the DNL structure along the Y to M point protected by a glide reflection $\bar{M}_{010}$ = $\{M_{010}|0,1/2,0\}$. Along the Y–M lines, (k_x,π), the eigenvalues of the glide symmetry $\bar{M}_{010}$ are given by $g_\pm(\mathbf{k}) = m_\pm\phi(\mathbf{k}) = \pm e^{-ik_y/2} = \pm i$,[41] where $m_\pm = \pm 1$ is the spinless eigenvalues of the mirror reflection symmetry M_{010}, and $\phi(\mathbf{k}) = e^{-ik_y/2}$ is the phase factor induced by the fractional translation. Since the lowest conduction band and the highest valence band have opposite signs of eigenvalues with respect to the glide symmetry $\bar{M}_{010}$, the band crossings between these two bands do not open a gap on the Y–M line. Moreover, since the time-reversal symmetry T commutes with $\bar{M}_{010}$, *i.e.* $[\bar{M}_{010}, T] = 0$, it leads to

$$\begin{aligned} \bar{M}_{010}(T|\psi_k\rangle) &= T(\bar{M}_{010}|\psi_k\rangle) \\ &= T(\pm i|\psi_k\rangle) = \pm iT|\psi_k\rangle. \end{aligned} \quad (3)$$

Thus, $|\psi_k\rangle$ and $T|\psi_k\rangle$ have the same $\bar{M}_{010}$ eigenvalues of $\pm i$. This also makes the band crossing points on the Y–M line protected to form a line with four-fold degeneracy. The DNL here is an essential nodal line and not an accidental nodal line. As an interesting electronic property of the 2D DNL structure, it has a significantly different DOS from the 2D Dirac state ($D(E) \propto |E - E_F|$). For DNL semimetals with band crossing occurring on a 1D line, the effective energy dispersion is given by $E(\mathbf{k})$ =

$\pm\hbar v_F k_x + \cos(k_y)$. One can calculate the DOS of the DNL system as

$$D(E) = \frac{g}{(2\pi)^2}\int d^2k\delta(E - E(k)) = \frac{g}{(2\pi)^2}\int_{k_x}\int_{k_y} \mathrm{d}k_x\mathrm{d}k_y\delta(E - \hbar v_F k_x - \cos\, k_y) = \frac{g}{\hbar v_F(2\pi)^2}, \quad (4)$$

where g is the degeneracy factor. The DOS of the 1D DNL state does not depend on energy, as clearly seen from the constant DOS in DFT and TB model results [Fig. 1(d) and 2(e)]. Due to its unique DNL and constant DOS, the collective mode of plasma oscillation[42,43] can be realized (Fig. S4†).

Next, we move to other VA group elements (As, Sb and Bi) which have strong SOC. Fig. 3(a) and (b) show fluorinated (As–F, Sb–F and Bi–F) and chlorinated (As–Cl, Sb–Cl and Bi–Cl) phosphorene structures made of these elements. The DNL structure becomes a Weyl nodal line due to SOC and the broken inversion symmetry. Without SOC, other group VA elements also have the DNL structure along the Y–M lines (Fig. S5†). Comparing the band structures calculated with SOC [Fig. 3(a) and (b)] and without SOC (Fig. S5†), a sizable band spin splitting produced by the Rashba SOC is seen at some high symmetry k points and along certain k paths. At the Y and M points, the Dirac points are doublets resulting from the Rashba SOC splitting. The splitting are ~2 meV, ~40 meV and ~140 meV for As–F, Sb–F and Bi–F, respectively. The bands along the Y–M line are doubly degenerate protected by T and $\bar{M}_{010} = \{M_{100}|0,1/2,0\}$. Along this line $\mathbf{k} = (k_x,\pi)$, k_x is invariant under the transformations $\bar{M}_{010}$ and $\Theta = T\bar{M}_{100}$. Since $T^2 = -1$ for a spin-half system, we find $\Theta^2 = T^2\bar{M}_{100}{}^2 = e^{-ik_y} = -1$, and all bands are doubly degenerate along the Y–M line. The doublet states $(\psi_k,\Theta\psi_k)$ form a Kramers pair. Moreover, one can understand the lifting of the degeneracy along the Γ–Y line, where $\mathbf{k} = (0,k_y)$, from the group symmetries $\bar{M}_{100}$ and $\tilde{\Theta} \equiv T\bar{M}_{010}$. Along the Γ–Y line, $\tilde{\Theta}^2 = T^2\bar{M}_{010}{}^2 = 1$ and hence the Bloch states ψ_k and $\Theta\psi_k$ are not degenerate. In addition, each state can be labeled using the eigenvalues of $\bar{M}_{100}$. Since $\bar{M}_{100}{}^2 = -e^{-ik_y}$, one has $\bar{M}_{100}|\psi_k^{\pm}\rangle = \pm ie^{-ik_y/2}|\psi_k^{\pm}\rangle$. Consequently, $\bar{M}_{100}$ has eigenvalues $\pm i$ at the Γ point and eigenvalues ±1 at the Y point [last panel of Fig. 3(b)]. This in turn amounts to four non-degenerate Bloch states. Interestingly, the crossing of the $\psi_k{}^+$ and $\psi_k{}^-$ bands is enforced and protected by the $\bar{M}_{100}$ symmetry and is robust against SOC, resulting in the hourglass-shaped band dispersion.[6,44] The feature of the constant DOS appears for other VA elements except for Sb–F and Bi–F, which has additional contribution from the p_z-orbital states at the X point (Fig. S6†).

Fig. 4(a) shows the 3D band structure along the Y–M lines for the Bi–Cl structure displaying the hourglass dispersion. In contrast to DNL for the spinless case, Weyl points generically occur at the low-symmetry k points. Specifically, we find two pairs of Weyl points located along the Γ–Y and X–M lines. To demonstrate the existence of Weyl points and to pinpoint their location in $\mathbf{k}$ space, we calculate the band structure on a dense k grid and show the energy difference between the conduction and valence bands in Fig. 4(b) on a logarithmic scale, *i.e.*, $\log_{10}(E_{cb} - E_{vb})$. This clearly shows the two pairs of Weyl points $W_1{}^{\pm}$ and $W_2{}^{\pm}$, symmetrically displaced from the Y–M line. To describe the hourglass dispersion, we considered the Rashba interaction induced by the broken inversion symmetry and strong SOC in the effective model Hamiltonian. We apply an effective electric field perpendicular to the layer plane. The Rashba Hamiltonian is given by

$$H_R = i\lambda_R\sum_{\langle ij\rangle} c_i{}^+(\boldsymbol{\sigma}\times\hat{\mathbf{d}}_{ij})c_j, \quad (5)$$

where $\hat{\mathbf{d}}_{ij}$ is the unit vector going from site j to i. In Fig. 4(c) we show the band structure of the effective model with the Rashba field. The hourglass structure along the Γ–Y and X–M lines is well reproduced by the effective model.

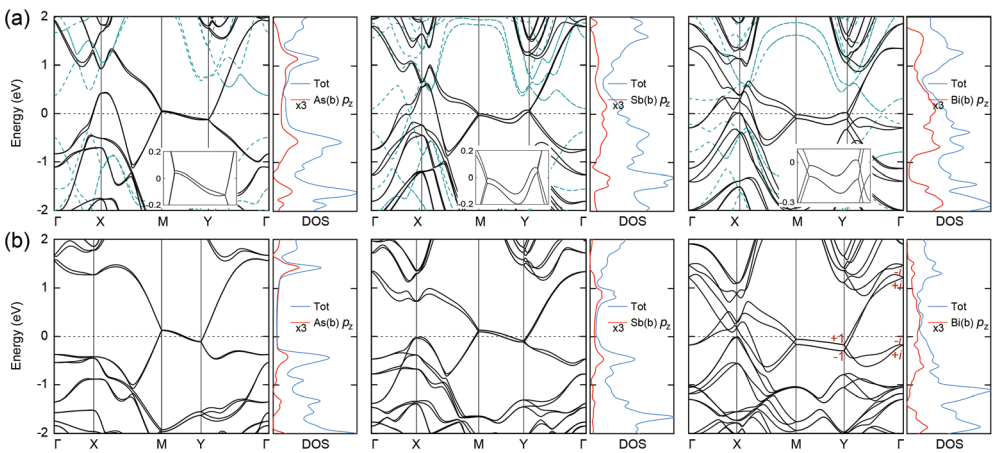

Fig. 3 (a) The calculated band structures and density of states for As–F, Sb–F and Bi–F, respectively. The band structure for the pristine group VA phosphorene structure is indicated by the dashed line. (b) The calculated band structure and density of states for As–Cl, Sb–Cl and Bi–Cl, respectively.

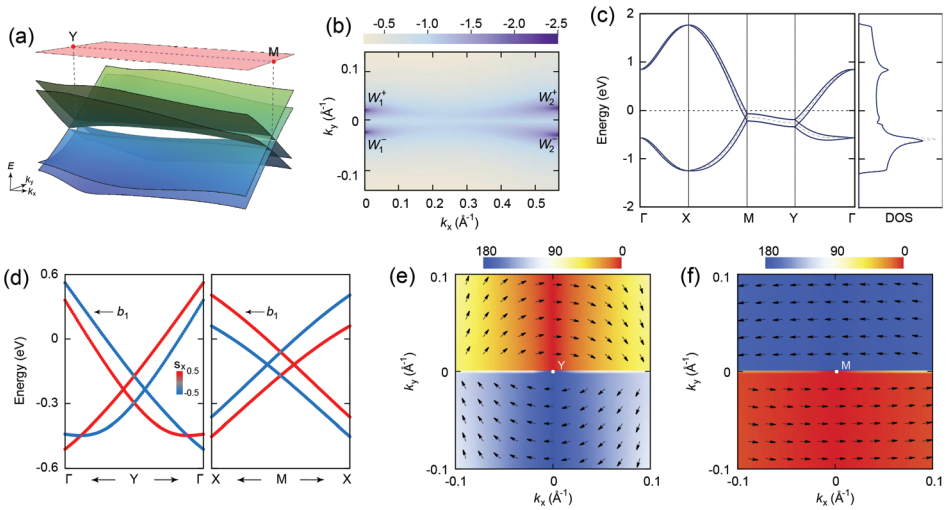

Fig. 4 (a) The 3D band structure for Bi–Cl along the Y–M direction as indicated by a small shaded rectangle in Fig. 1(c). (b) Color map of energy difference between the conduction and valence bands on the logarithmic scale $\log_{10}(E_{cb} - E_{vb})$, where $W_1^{\pm}$ and $W_2^{\pm}$ denote the Weyl points. (c) The band structure of the effective Hamiltonian using two p_z orbitals with the Rashba SOC interaction. (d) Band structure near the Y and M points with the spin configuration of the x component. (e), (f) Spin configurations of the b_1 band in (d) around the high-symmetry k points: Y point (e) and M point (f). The values at Y and M points are set to be zero, respectively. The color map reflects the polar angle (in degrees) with respect to the x-axis.

Next, we examine the spin texture around the Y and M points. Fig. 4(d) shows the band structure of Bi–Cl with the spin polarization information near the Y and M points. The spin component of bands has the in-plane (x-direction) component only. It can be understood from the symmetry analysis. At the Y point, $\bar{M}_{100}$ commutes with the system Hamiltonian, $[\bar{M}_{100},H] = 0$, and the doublet $(\psi_Y,\Theta\psi_Y)$ can be labeled using the eigenvalues of $\bar{M}_{100}$. Since $\bar{M}_{100}{}^2 = 1$ at the Y point, we have $\bar{M}_{100}|\psi_Y^{\pm}\rangle = \pm|\psi_Y^{\pm}\rangle$ and $\bar{M}_{100}\Theta|\psi_Y^{\pm}\rangle = \pm\Theta|\psi_Y^{\pm}\rangle$. Thus, by symmetry, there are two conjugated doublets, $(\psi_Y{}^+,\Theta\psi_Y{}^+)$ or $(\psi_Y{}^-,\Theta\psi_Y{}^-)$, which are distinguishable by the $\bar{M}_{100}$ eigenvalues. Within each of the two doublets, matrix elements of the spin operators σ_y and σ_z are equal to zero. This is due to the fact that $\bar{M}_{100}$ anticommutes with σ_y and σ_z, which results in $\langle\psi_Y{}^+|\sigma_{y,z}|\psi_Y{}^+\rangle = \langle\psi_Y{}^+|\bar{M}_{100}\sigma_{y,z}\bar{M}_{100}|\psi_Y{}^+\rangle = -\langle\psi_Y{}^+|\sigma_{y,z}|\psi_Y{}^+\rangle$ and hence $\langle\psi_Y{}^+|\sigma_{y,z}|\psi_Y{}^+\rangle = 0$. A similar analysis leads to $\langle\Theta\psi_Y{}^+|\sigma_{y,z}|\Theta\psi_Y{}^+\rangle = 0$ and $\langle\psi_Y{}^+|\sigma_{y,z}|\Theta\psi_Y{}^+\rangle = 0$. The same conclusion holds for the other doublet $(\psi_Y{}^-,\Theta\psi_Y{}^-)$. Therefore, any state, which represents a linear combination of the states comprising either doublet, $|\psi_k^{\pm}\rangle = \eta_k|\psi_Y^{\pm}\rangle + \chi_k|\Theta\psi_Y^{\pm}\rangle$, has zero expectation values of $\sigma_{y,z}$. Thus the only nonzero component of the spin is σ_x, and the spin orientation is forced to be along the x-direction. A similar analysis applies to the M point.

When moving away from the Y or M point the perturbation breaks the symmetry and further splits the doublets. If the perturbation is not too strong to mix the doublets, the spin textures are preserved along the x-direction. Fig. 4(e) and (f) show the calculated spin textures around the Y and M points for the conduction band [indicated by b_1 in Fig. 4(d)]. One can see a unidirectional spin configuration for positive and negative values of k_y (referred to the origin of the Y point and M point). The spin orientation changes abruptly at $k_y = 0$, where the x component of the spin is reversed. The spin texture around the Y and M points shows a similar trend but the spin direction is opposite. There is a visible deviation from the unidirectional spin orientation when moving away from the Y point due to the mixing of the doublets.

For the experimental realization of the chemically modified 2D group VA puckered structure, one needs to find a benign substrate that provides stable mechanical support yet retains the Dirac semimetal properties. Recent studies showed that van der Waals (vdW) heterostructures combining monolayer black phosphorene and other 2D materials, such as graphene,[45] hexagonal boron nitride (BN)[46] and transition-metal dichalcogenides (TMDs),[47] can protect the desirable electronic properties of phosphorene. It is reasonable to expect that the chemically modified group-VA puckered structure can also be synthesized on some substrates with vdW interactions by various techniques, including mechanical exfoliation and molecular beam epitaxy. To test this hypothesis, we use BN sheets as a substrate to support As–F (Fig. S7†). The As–F on the BN sheets retains the DNL structure, there is essentially no charge transfer between the adjacent layers, and the DNL states around the Fermi level are dominantly contributed by the As p_z orbitals of the bottom layer.

Conclusions

In summary, based on first-principles calculations and model analysis, we predict an intriguing 2D Dirac and Weyl state protected by a nonsymmorphic group symmetry in a chemically modified group-VA 2D puckered structure. The DNL structure forms along the high-symmetry lines in the absence of SOC.

When SOC is strong, the DNLs split and form the hourglass dispersion, which is protected by the nonsymmorphic symmetry. We further show that the unidirectional spin textures are derived from the interplay between SOC and glide reflection symmetries. Our finding suggests a new platform to explore novel types of 2D Dirac fermions both for their fascinating fundamental properties and promising device applications.

Conflicts of interest

There are no conflicts to declare.

Acknowledgements

K. H. J., H. H. and F. L. acknowledge financial support from U.S. DOE-BES (No. DE-FG02-04ER46148). The calculations were done on the CHPC at the University of Utah and DOE-NERSC.

References

1 K. S. Novoselov, A. K. Geim, S. V. Morozov, D. Jiang, M. I. Katsnelson, I. V. Grigorieva, S. V. Dubonos and A. A. Firsov, *Nature*, 2005, **438**, 197.
2 M. Z. Hasan and C. L. Kane, *Rev. Mod. Phys.*, 2010, **82**, 3045–3067.
3 S. M. Young, S. Zaheer, J. C. Y. Teo, C. L. Kane, E. J. Mele and A. M. Rappe, *Phys. Rev. Lett.*, 2012, **108**, 140405.
4 B. Yan and C. Felser, *Annu. Rev. Condens. Matter Phys.*, 2017, **8**, 337–354.
5 C. L. Kane and E. J. Mele, *Phys. Rev. Lett.*, 2005, **95**, 226801.
6 S. M. Young and C. L. Kane, *Phys. Rev. Lett.*, 2015, **115**, 126803.
7 S. Guan, Y. Liu, Z.-M. Yu, S.-S. Wang, Y. Yao and S. A. Yang, *Phys. Rev. Mater.*, 2017, **1**, 054003.
8 H. Liu, A. T. Neal, Z. Zhu, Z. Luo, X. Xu, D. Tománek and P. D. Ye, *ACS Nano*, 2014, **8**, 4033–4041.
9 A. Carvalho, M. Wang, X. Zhu, A. S. Rodin, H. Su and A. H. Castro Neto, *Nat. Rev. Mater.*, 2016, **1**, 16061.
10 X. Li, L. Ma, D. Wang, X. C. Zeng, X. Wu and J. Yang, *Nanoscale*, 2016, **8**, 17801–17808.
11 M. Qiu, Z. T. Sun, D. K. Sang, X. G. Han, H. Zhang and C. M. Niu, *Nanoscale*, 2017, **9**, 13384–13403.
12 H. Liu, J.-T. Sun, C. Cheng, F. Liu and S. Meng, *Phys. Rev. Lett.*, 2018, **120**, 237403.
13 C. Kamal and M. Ezawa, *Phys. Rev. B: Condens. Matter Mater. Phys.*, 2015, **91**, 085423.
14 G. Wang, R. Pandey and S. P. Karna, *ACS Appl. Mater. Interfaces*, 2015, **7**, 11490–11496.
15 O. Ü. Aktürk, V. O. Özçelik and S. Ciraci, *Phys. Rev. B: Condens. Matter Mater. Phys.*, 2015, **91**, 235446.
16 M. Pumera and Z. Sofer, *Adv. Mater.*, 2017, **29**, 1605299.
17 Y. Lu, D. Zhou, G. Chang, S. Guan, W. Chen, Y. Jiang, J. Jiang, X.-s. Wang, S. A. Yang, Y. P. Feng, Y. Kawazoe and H. Lin, *npj Comput. Mater.*, 2016, **2**, 16011.
18 T. Märkl, P. J. Kowalczyk, M. L. Ster, I. V. Mahajan, H. Pirie, Z. Ahmed, G. Bian, X. Wang, T. C. Chiang and S. A. Brown, *2D Mater.*, 2018, **5**, 011002.
19 Y. Lu, W. Xu, M. Zeng, G. Yao, L. Shen, M. Yang, Z. Luo, F. Pan, K. Wu, T. Das, P. He, J. Jiang, J. Martin, Y. P. Feng, H. Lin and X.-s. Wang, *Nano Lett.*, 2015, **15**, 80–87.
20 R. Fei and L. Yang, *Nano Lett.*, 2014, **14**, 2884–2889.
21 V. Tran, R. Soklaski, Y. Liang and L. Yang, *Phys. Rev. B: Condens. Matter Mater. Phys.*, 2014, **89**, 235319.
22 Y. Hong, J. Zhang, X. Huang and X. C. Zeng, *Nanoscale*, 2015, **7**, 18716–18724.
23 P. Zhang, Z. Liu, W. Duan, F. Liu and J. Wu, *Phys. Rev. B: Condens. Matter Mater. Phys.*, 2012, **85**, 201410.
24 S. H. Kim, K.-H. Jin, J. Park, J. S. Kim, S.-H. Jhi and H. W. Yeom, *Sci. Rep.*, 2016, **6**, 33193.
25 S. H. Kim, K.-H. Jin, B. W. Kho, B.-G. Park, F. Liu, J. S. Kim and H. W. Yeom, *ACS Nano*, 2017, **11**, 9671–9677.
26 S. Murakami, *Phys. Rev. Lett.*, 2006, **97**, 236805.
27 Z. Liu, C.-X. Liu, Y.-S. Wu, W.-H. Duan, F. Liu and J. Wu, *Phys. Rev. Lett.*, 2011, **107**, 136805.
28 F. Yang, L. Miao, Z. F. Wang, M.-Y. Yao, F. Zhu, Y. R. Song, M.-X. Wang, J.-P. Xu, A. V. Fedorov, Z. Sun, G. B. Zhang, C. Liu, F. Liu, D. Qian, C. L. Gao and J.-F. Jia, *Phys. Rev. Lett.*, 2012, **109**, 016801.
29 S. H. Kim, K.-H. Jin, J. Park, J. S. Kim, S.-H. Jhi, T.-H. Kim and H. W. Yeom, *Phys. Rev. B: Condens. Matter Mater. Phys.*, 2014, **89**, 155436.
30 Z. F. Wang, L. Chen and F. Liu, *Nano Lett.*, 2014, **14**, 2879–2883.
31 K.-H. Jin and S.-H. Jhi, *Sci. Rep.*, 2015, **5**, 8426.
32 K.-H. Jin and S.-H. Jhi, *Phys. Chem. Chem. Phys.*, 2016, **18**, 8637–8642.
33 G. Wang, R. Pandey and S. P. Karna, *Nanoscale*, 2015, **7**, 524–531.
34 C. R. Ryder, J. D. Wood, S. A. Wells, Y. Yang, D. Jariwala, T. J. Marks, G. C. Schatz and M. C. Hersam, *Nat. Chem.*, 2016, **8**, 597.
35 Y. Ma, Y. Dai, L. Kou, T. Frauenheim and T. Heine, *Nano Lett.*, 2015, **15**, 1083–1089.
36 G. Kresse and J. Furthmüller, *Phys. Rev. B: Condens. Matter Mater. Phys.*, 1996, **54**, 11169–11186.
37 J. P. Perdew, K. Burke and M. Ernzerhof, *Phys. Rev. Lett.*, 1996, **77**, 3865–3868.
38 A. Togo and I. Tanaka, *Scr. Mater.*, 2015, **108**, 1–5.
39 V. V. Kulish, O. I. Malyi, C. Persson and P. Wu, *Phys. Chem. Chem. Phys.*, 2015, **17**, 992–1000.
40 D. Yu and F. Liu, *Nano Lett.*, 2007, **7**, 3046–3050.
41 B.-J. Yang, T. A. Bojesen, T. Morimoto and A. Furusaki, *Phys. Rev. B: Condens. Matter Mater. Phys.*, 2017, **95**, 075135.
42 Z. F. Wang and F. Liu, *Phys. Rev. Lett.*, 2015, **115**, 026803.
43 J. Wang, Y. Liu, K.-H. Jin, X. Sui, L. Zhang, W. Duan, F. Liu and B. Huang, *Phys. Rev. B: Condens. Matter Mater. Phys.*, 2018, **98**, 201112.

44 Z. Wang, A. Alexandradinata, R. J. Cava and B. A. Bernevig, *Nature*, 2016, **532**, 189.
45 Y. Cai, G. Zhang and Y.-W. Zhang, *J. Phys. Chem.*, 2015, **119**, 13929–13936.
46 G. C. Constantinescu and N. D. M. Hine, *Nano Lett.*, 2016, **16**, 2586–2594.
47 B. You, X. Wang, Z. Zheng and W. Mi, *Phys. Chem. Chem. Phys.*, 2016, **18**, 7381–7388.